Molecular Physics, Vol. 104, No. 8, 20 April 2006, 1249–1266

Taylor & Francis
Taylor & Francis Group

Quantum logic gates in iodine vapor using time–frequency resolved coherent anti-Stokes Raman scattering: a theoretical study

DAVID R. GLENN*†§, DANIEL A. LIDAR† and V. ARA APKARIAN‡

†Chemical Physics Theory Group, Chemistry Department, University of Toronto,
80 St. George St., Toronto, Ontario M5S 3H6, Canada
‡Chemistry Department, University of California, 516 Rowland Hall,
Irvine, CA 92697-2025, USA

(*Received 14 July 2005; in final form 5 October 2005*)

We present a numerical investigation of the implementation of quantum logic gates through time–frequency resolved coherent anti-Stokes Raman scattering (TFRCARS) in iodine vapour. A specific scheme is given whereby two qubits are encoded in the tensor product space of vibrational and rotational molecular eigenstates. Single-qubit and controlled-logic gates are applied to test the viability of this encoding scheme. Possible experimental constraints are investigated, including the necessary precision in the timing of successive CARS pulses and the minimum resolution of spectral components within a given pulse. It is found that these requirements can be satisfied by current technology. The two-qubit Grover search is performed to demonstrate the implementation of a sequence of quantum operations. The results of our simulations suggest that TFRCARS is a promising experimental system for simple quantum information processing applications.

Keywords: Quantum logic gates; Iodine vapour; Time–frequency resolved coherent anti-Stokes Raman scattering

1. Introduction

Interest in the study of quantum information and quantum computation has increased tremendously in the past decade. The origin of the field is commonly attributed to Feynman [1], who proposed that one quantum mechanical system could be used to efficiently simulate others. Benioff [2] and Deutsch [3] also made important early contributions to our understanding of the relationship between classical and quantum computation. The recent surge in activity is due in large part to the development of important quantum algorithms by Shor [4] and Grover [5]. The former provides a method for factoring large numbers into primes that scales polynomially in the number of digits. The latter allows a search through a list of N elements to be conducted in $O(N^{1/2})$ steps, which is provably faster than the best possible classical algorithm.

Numerous candidate systems have been suggested for the physical implementation of a quantum computer. The problem is a challenging one, due to the intrinsic trade-off between long decoherence times and the ease with which quantum states may be prepared and measured. The proposals that have been experimentally demonstrated to date are liquid-state NMR [6], cavity QED [7], cold trapped ions [8] superconducting tunnel junctions [9], and quantum dots [10]. A number of recent studies have focussed on the possibility of encoding quantum bits into molecular states that can be manipulated through nonlinear optical interactions [11–14].

The present investigation explores the use of time–frequency resolved coherent anti-Stokes Raman scattering (TFRCARS) to create and manipulate ro-vibronic coherences in molecular iodine vapour. It has been shown that the structure of time-resolved CARS gives access to the operations necessary for universal quantum computation, namely arbitrary

---

*Corresponding author. Email: david.glenn@yale.edu

§Present address: Department of Physics, Yale University, Sloane Physics Lab, 217 Prospect Street, New Haven, Connecticut 06511-8499, USA.

Molecular Physics
ISSN 0026–8976 print/ISSN 1362–3028 online
http://www.tandf.co.uk/journals
DOI: 10.1080/00268970500525713

single-qubit rotations and a two-qubit controlled-NOT gate [11]. Previous calculations have demonstrated how a coherent computation can be carried out with TFRCARS on the vibrational states of I_2 [12]. This research extends those results by developing a numerical simulation of the system in the full ro-vibronic Hilbert space, consisting of the tensor products of Born–Oppenheimer separated electronic, vibrational, and rotational states.

This paper is structured as follows. In section 2, we provide a brief overview of the experimental CARS system, and the theoretical methodology of double-sided Feynman diagrams used to describe this system. In section 3 we describe our simulations and scheme for encoding quantum information into electronic and ro-vibrational states. In section 4 we present our results on a simple quantum algorithm implemented using TFR-CARS in iodine. We conclude in section 5.

2. The system

Here, we give a physical description of the CARS system. Relevant references include [11, 15, 16], as well as Mukamel's text on nonlinear optics [17], several general texts on molecular spectroscopy [18–20], and a number of other papers on modeling CARS systems [21–23].

2.1. *The experiment*

The numerical simulation we present later is modeled after ongoing experiments being carried out in the Apkarian group. A schematic representation of the apparatus, taken directly from one of their recent papers [15], is shown in figure 1. The I_2 vapour resides in a quartz cell at 0.3 Torr, heated to 50°C. Three phase-locked, linearly polarized optical pulses interact successively with the molecules over a time interval on the order of tens to hundreds of picoseconds. These pulses establish and manipulate the quantum coherences used to perform the computation. In the standard CARS nomenclature, the pulses are named according to the order in which they interact with the system: The first is labelled P, for 'pump'; the second S, for 'Stokes', because it is traditionally tuned to the red of the first pulse; and the third P′, either for 'probe', or because it is often the same colour as the first pulse. These pulses are initially generated by a Ti:sapphire laser, with its output compressed to 70 fs and 700 μJ/pulse by chirped pulse amplification. This is split to two optical parametric amplifiers (OPA), the outputs of which are up-converted by sum generation to be tuneable in the near infrared, 480–2000 nm. The P and P′ pulses are obtained by splitting the output of one OPA, while the second OPA generates the S pulse. The spectrum of each pulse is precisely shaped using a spatial light modulator before it interacts with the sample. All pulses are chosen to be resonant with the dipole allowed $X(^1\sum_{0g+})\leftrightarrow B(^3\prod_{0u+})$ electronic transition.

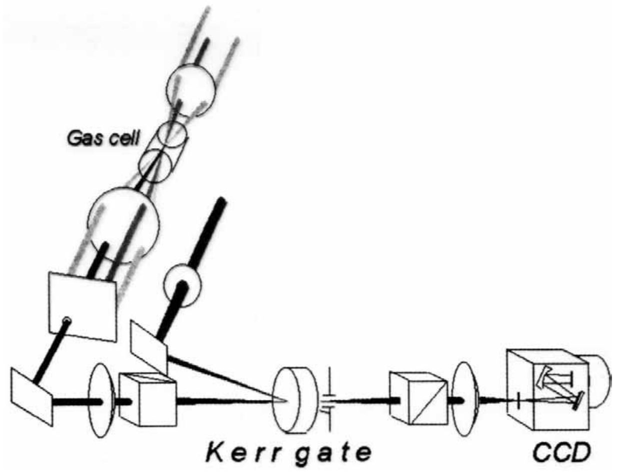

Figure 1. Experiment schematic—from [13].

The part of the macroscopic polarization due to the subset of iodine molecules that interact exactly once with each pulse generates the experimental signal. This is the so-called AS, or 'anti-Stokes' radiation. It is separated from the other scattered light by spatially filtering along the direction of the anti-Stokes wave-vector, $\mathbf{k}_{AS} = \mathbf{k}_P - \mathbf{k}_S + \mathbf{k}_{P'}$, which corresponds to the CARS energy conservation condition $\omega_{AS} = \omega_P - \omega_S + \omega_{P'}$. The anti-Stokes signal is precisely truncated in time by passing it through a pair of cross-polarized prisms surrounding a Kerr cell. Rotation is induced in the cell by a small fraction of the original 800 nm fundamental Ti:sapphire output, which has been polarized at 45° to the AS radiation and timed with a delay line. The resulting AS pulse is dispersed in a monochromator and directed onto a CCD array for detection.

2.2. *Calculating the molecular polarization*

Evolution of molecular states under the influence of the applied pulses is calculated in the time domain, using the formalism of time-dependent perturbation theory. The interaction Hamiltonian is described semi-classically and in the dipole approximation,

$$H_I(t) = -\mu \cdot E(t). \tag{1}$$

For the perturbative approach to be valid, the field must be weak: $\mu E_0 \tau \ll \hbar$, where E_0 is the average amplitude of the pulse and τ its duration. This requirement is satisfied in the experiment.

The molecular states are written in the interaction picture, where the usual procedure of iterative integration leads to the following time evolution operator:

$$U(t,t_0) = U_0(t,t_0) + \sum_{n=1}^{\infty} \left(\frac{-i}{\hbar}\right)^n \int_{t_0}^{t} \mathrm{d}\tau_n \int_{t_0}^{\tau_n} \mathrm{d}\tau_{n-1} \cdots \int_{t_0}^{\tau_2} \mathrm{d}\tau_1$$

$$(U_0(t,\tau_n) H_{\mathrm{I}}(\tau_n) U_0(\tau_n,\tau_{n-1})$$

$$H_I(\tau_{n-1}) \cdots U_0(\tau_2,\tau_1) H_{\mathrm{I}}(\tau_1) U_0(\tau_1,t_0)). \tag{2}$$

The operator U_0 describes evolution under the free molecular Hamiltonian H_0. Since we are concerned only with states which undergo exactly three interactions with the electromagnetic field, the sum can be truncated at $n = 3$.

The expression for the matrix elements of the molecular polarization, at third order, is given by

$$P^{(3)}(t) = \langle \psi^{(3)}(t) | \mu | \psi^{(0)}(t) \rangle + \langle \psi^{(2)}(t) | \mu | \psi^{(1)}(t) \rangle + \text{c.c.} \tag{3}$$

Here, $|\psi^{(j)}(t)\rangle$ is obtained by applying the jth term in the sum from equation (2) to the initial state $|\psi(t0)\rangle$. The expression for $P^{(3)}$ is summed over all molecules to obtain the macroscopic polarization, which acts as a source in Maxwell's equations. The observed field, E_{AS}, is therefore directly proportional to $P^{(3)}$.

In the simplest case, the expression in equation (3) contains four terms. When the dipole Hamiltonian in (1) is substituted into (2), indices must be added to the E field to distinguish the three pulses: E_{P}, E_{S}, $E_{\mathrm{P'}}$. Because of the spatial filtering in the experiment, it is guaranteed that the system will interact with each pulse exactly once. However, if the pulses overlap temporally, multiple time orderings may be possible in the evaluation of (2). In principle, all permutations of the three pulse indices must be calculated, increasing the total number of terms in (3) to 24. Practically, most of these terms will be almost zero except where, for instance, $E_{\mathrm{P}}(t)$ and $E_{\mathrm{S}}(t)$ both have non-negligible amplitudes for the same value of t.

It is common to use time circuit diagrams to depict each of the terms of equation (3). Examples of such diagrams are illustrated in figure 2. The horizontal direction represents time, while the vertical describes the energy of the state. In the Born–Oppenheimer approximation, states shown above the dotted line are ro-vibrational levels in the excited (B) electronic state, while those below the line are in the ground (X) electronic state. Each diagram illustrates the interactions undergone by both the bra $|\psi^{(j)}\rangle$ and the ket $\langle\psi^{(j-3)}|$. Figure 2(b), for instance, describes the following sequence. (i) The ket interacts with the P pulse at t_1 and is excited from the X to the B electronic state. (ii) The bra interacts successively with the S pulse at t_2 and the P′ pulse at t_3, remaining on the B surface during the interval between those pulses. (iii) At some later time t the coherence between the bra and ket spontaneously collapses, and a photon is emitted which will contribute to the AS radiation. This contribution adds to the term denoted $\langle\psi^{(2)}(t)|\mu|\psi^{(1)}(t)\rangle$ in equation (3).

Of the three diagrams displayed, only the one in figure 2(a) typically makes a significant contribution to the macroscopic polarization. The diagram in figure 2(b) is suppressed because it begins from an excited initial level, which will have a smaller amplitude than the vibrational ground state in a thermal distribution. The diagram in figure 2(c) will not contribute significantly because the transition excited by the P′ pulse is not resonant. The full integral expression for the contribution from figure 2(a) is as follows [23]:

$$P_{\mathrm{AS}}^{(0,3)}(t) = \frac{k}{\hbar^3} \int_{-\infty}^{t} \mathrm{d}t_3 \int_{-\infty}^{t_3} \mathrm{d}t_2 \int_{-\infty}^{t_2} \mathrm{d}t_1$$

$$\left\langle \psi\, \mathrm{e}^{(i/\hbar) H_{\mathrm{X}} t} |\mu|\, \mathrm{e}^{(-i/\hbar) H_{\mathrm{B}}(t-t_3)} \mu \cdot E_{\mathrm{P'}}(t_3)\, \mathrm{e}^{(-i/\hbar) H_{\mathrm{X}}(t_3-t_2)} \mu \right.$$

$$\left. \cdot E_{\mathrm{S}}^{*}(t_2)\, \mathrm{e}^{(-i/\hbar) H_{\mathrm{B}}(t_2-t_1)} \mu \cdot E_{\mathrm{P}}(t_1)\, \mathrm{e}^{(-i/\hbar) H_{\mathrm{X}} t_1} \psi \right\rangle + \text{c.c.} \tag{4}$$

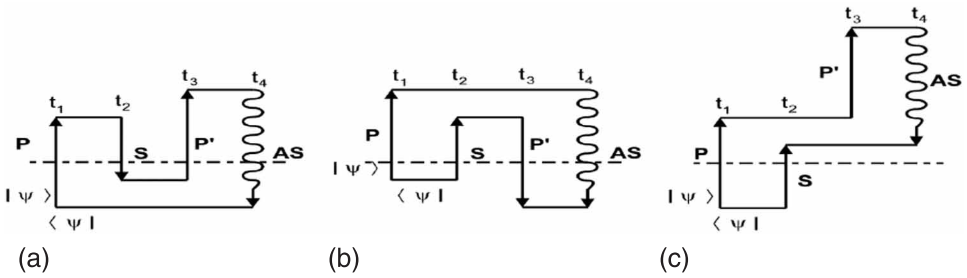

Figure 2. Sample time-circuit diagrams.

Evaluation of the dipole matrix elements is performed in the Franck–Condon limit, so that μ in equation (4) may effectively be replaced by the product of the spatial overlap of the initial and final vibrational wavefunctions and a constant associated with the X and B electronic states. This must be multiplied by a rotational matrix element [20] to account for all possible magnetic quantum numbers when the interaction with a linearly polarized field changes the total angular momentum of the state by ±1. Thus, the complete expression for the dipole matrix element between Born–Oppenheimer separated states of the form $\phi^{e,v,J}$ is given by

$$\left\langle \phi^{e,v,J} | \mu | \phi^{e',v',J\pm1} \right\rangle = \mu_{e,e'} \left\langle \nu(\mathbf{r}) | \nu'(\mathbf{r}) \right\rangle D_{j,\,j\pm1}, \tag{5}$$

where the rotational matrix element is the sum over Clebsch–Gordan coefficients

$$D_{j,j\pm1} = \sum_{m=-j}^{j} \left\langle j,m;\ 1,0 | j \pm 1, m \right\rangle. \tag{6}$$

It can be shown [23] that the time domain representation of the contribution to the polarization in equation (4) is equivalent to a more commonly encountered frequency domain expression involving the so-called hyperpolarizability tensor, γ:

$$P_{\rho}^{(3)}(\omega z_0) = \gamma_{\rho\sigma\tau\upsilon} E^{\sigma}(\omega_1) E^{\tau}(\omega_2) E^{\upsilon}(\omega_3) \delta(\omega_1 - \omega_2 + \omega_3 - \omega_0). \tag{7}$$

Furthermore, Mukamel shows [17] that expression (4) is equivalent, for a pure initial state, to his more complicated general expression involving density operators evolving in Liouville space. Although the initial state of the physical system is actually a thermal distribution, it turns out that this simplification is still valid for our purposes. The reason is that, for a pump pulse with sufficient spectral selectivity, only one state in the initial thermal distribution actually contributes to the evolving coherence. This is demonstrated numerically in section 4.3.

It is important to note that equation (4) represents the contribution of a single molecule to the bulk polarization. A macroscopic ensemble of these molecules produces the anti-Stokes radiation, where each spontaneous emission event is effectively a measurement of an independent single-particle wavefunction. Observation of the AS pulse in the frequency domain is therefore equivalent to complete tomography of the segment of the molecular density matrix that describes the third-order coherence. For quantum information processing applications, the state of the qubits is encoded in the evolving coherence. A single pulse sequence performs the same quantum computation on many molecules in parallel, and the complex amplitudes of the final qubit states may therefore be read directly from the anti-Stokes radiation.

2.3. *Useful pictures: vibrational wavepackets and interferometer diagrams*

Several intuitive pictures have been used to describe the evolving molecular coherence under the action of the CARS pulses. The simplest of these employs the language of vibrational wavepackets in the position representation, oscillating on an anharmonic potential. Figure 3 gives a diagrammatic portrayal of this picture, for the large amplitude path corresponding to equation (4) and figure 2(*a*). At time t_1, the P pulse interacts with the molecules in the electronic ground state (0) to produce a vibrational wavepacket (1) on the excited electronic potential. The shape of this packet is determined by the relevant Franck–Condon factors, and one often speaks of the Franck–Condon 'window' of bond-lengths at which a vertical transition may occur. This window is located near the turning points of the potential, where a classically oscillating object would spend most of its time. The excited packet evolves on the B electronic surface until the arrival of the S pulse at t_2. The part of the packet overlapping with the Stokes window then returns to the ground electronic state (2). (Note that the position of the window is influenced to some extent by the mean frequency of the pulse, which determines the locations of the turning points. This can, of course, be understood more precisely by decomposing the wavepackets into eigenstates of the vibrational potentials). The packet now continues to evolve until t_3, when the P′ pulse again transfers the portion overlapping its Franck–Condon window to the

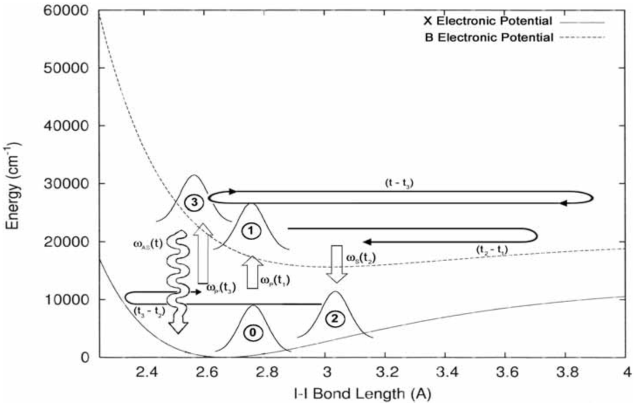

Figure 3. Vibrational wavepacket picture.

B electronic surface (3). The system is now in a third-order coherence, where all pulses have acted on the ket wavefunction and none on the bra. The excited wavepacket oscillates on the excited potential, radiating spontaneously every time it reaches the AS window at the inner turning point, corresponding to the energy conservation condition $\omega_{\mathrm{AS}} = \omega_{\mathrm{P}} - \omega_{\mathrm{S}} + \omega_{\mathrm{P'}}$. The macroscopic coherence persists until all molecules have emitted photons, or (more realistically) until it is destroyed by collisions.

The wavepacket picture assumes pulses of sufficient spectral width to transfer large superpositions of vibrational eigenstates. This situation is less than optimal for quantum information processing in the TFRCARS system, because it implies interference between the information-encoding states and those outside the computational space. Furthermore, wave packets become difficult to visualize when spherical harmonics are introduced to describe the rotational degree of freedom. An alternative description is therefore required. Figure 4 shows one possibility, where paths through Hilbert space involving particular pairs of vibrational states (or rotational states) are considered separately. Such diagrams draw attention to the phases acquired by individual eigenstates, with each pair of doubly intersecting paths effectively equivalent to a Mach–Zender interferometer in optics.

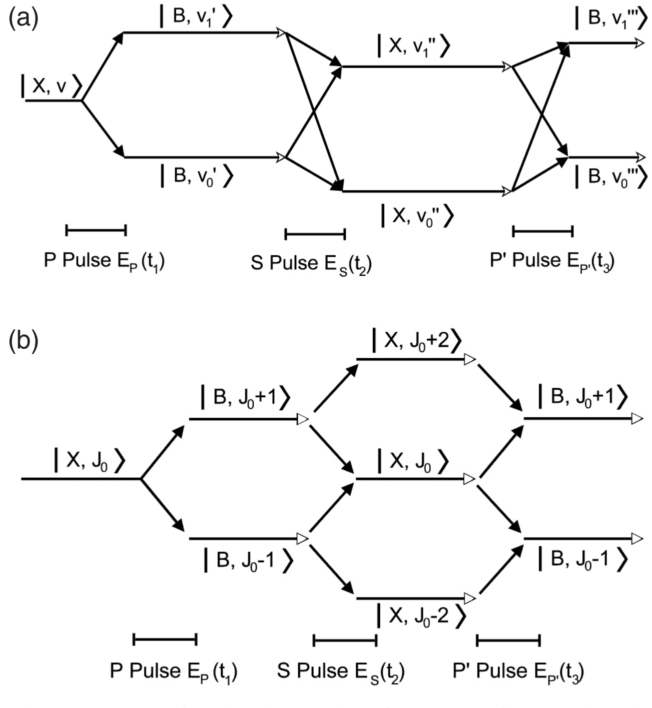

Figure 4. (a) Vibrational-state interferometer. (b) Rotational-state interferometer.

The interferometer diagram for the vibrational qubit is illustrated in figure 4(a). Solid diagonal arrows represent interactions with the electromagnetic field; open horizontal ones indicate evolution under the bare molecular Hamiltonian. In general, an arbitrary phase may be associated with each arrow, and an arbitrary amplitude with each one describing a field interaction. (In fact, in the limit of perfectly selective pulses, the phase acquired during free evolution is fixed; this will be discussed further in section 4.1). The vibrational quantum numbers of the states used to encode the $|0\rangle_v$ and $|1\rangle_v$ parts of the qubit at each step may be chosen freely by selecting appropriate frequencies for the spectral components of the pulses. Interference occurs whenever two non-zero diagonal arrows terminate in the same state. The total action on the vibrational qubit is therefore equivalent to two consecutive pairs of interlocking Mach–Zender interferometers, with each mirror capable of transmitting and reflecting the input signal at arbitrary phases, as well as freely attenuating or amplifying it.

Figure 4(b) shows the analogous diagram for the rotational qubit. Note that, in this case, dipole selection rules limit the allowed transitions, so that a more complex interferometer is required to effect the transformations desired for quantum information processing. Once again, the diagonal arrows represent pulse interactions, with which an arbitrary complex amplitude may be associated.

In the $v \otimes J$ tensor product representation, each path of the vibrational interferometer should have the components of the rotational interferometer for the relevant time interval superimposed on it. It can be shown that the interferometers depicted contain sufficient degrees of freedom to implement arbitrary SU(2) transformations on each of the qubits, given that the spectral components of the pulses are able to resolve rotational transitions independently. Deleting the appropriate arrows in the 'tensor-product of interferometers' may produce controlled operations, as long as the pulses are chosen so that each arrow corresponds to an independent spectral component. An important feature to notice in the interferometer diagrams is the freedom they allow in choosing the amplitude associated with each diagonal arrow. This underscores the fact that the transformations performed in the space of qubits are fundamentally non-unitary: doubling the amplitude of all spectral components of a given pulse will cause a corresponding doubling in the total amplitude of the output state. Normalization of the qubits must therefore be treated with some care. Finally, note that the diagrams of figure 4 illustrate the case where all three pulse-operators (i.e. $\mu \cdot E_i$) act on either the bra or the ket, as in figures 2(*a*) and 3. To represent other

Liouville paths, one could replace the appropriate pulses with zero-phase horizontal arrows.

3. Quantum logic gates using TFRCARS

We now describe how quantum information can be manipulated and processed using TFRCARS.

3.1. *Encoding qubits and quantum gates*

At the highest level of abstraction, the quantum computation consists of collection of three-pulse sequences, each of which represents a single quantum gate. Following the paradigm described in [11], the P pulse prepares the initial states of the qubits in the quantum register, the S pulse performs the desired transformation, and the P′ pulse prepares the system for readout. This procedure is repeated for each gate, until the full quantum algorithm has been implemented.

The P pulse consists of up to four spectral components, each of which excites a transition from some chosen original eigenstate in the thermal ensemble to an eigenstate encoding one of the tensor-product computational basis states. The original level on the ground electronic surface from which the computation is initiated may be chosen freely; the most common choice in our simulations has been $|\mathrm{X},\ v_0=0,\ J_0=52\rangle$, which has the maximum amplitude in a thermal distribution at 298 K. The vibrational quantum numbers of the encoding states are also arbitrary, although the rotational levels must be related to the original eigenstate by $\Delta J=\pm 1$. By convention the $|J_0+1\rangle$ states encode the $|1\rangle_J$ part of the rotational qubit, and the $|J_0-1\rangle$ states the $|0\rangle_J$ part. Likewise, the higher vibrational level typically encodes the $|1\rangle_v$ part of the vibrational qubit. The amplitude and phase of each component of the initial state are determined by the amplitude and phase of the corresponding P pulse component. In order to avoid contaminating the calculation by exciting transitions from initial thermal eigenstates other than the desired one (i.e. other than $|\mathrm{X},\ 0,\ 52\rangle$), the spectral components of the P pulse should be fairly narrow. In practice, it seems to be sufficient to choose the width of each component to be less than one-tenth the energy difference between the desired transition and the one connecting neighbouring rotational states. For instance, if the transition to be excited is $|\mathrm{X},\ v,\ J\rangle \rightarrow |\mathrm{B},\ v',\ J+1\rangle$, then the width of the pulse component, Γ, is chosen to satisfy

$$10\hbar\,\Gamma < \left|(E_{\mathrm{B},v',J+1}-E_{\mathrm{X},v,J})-(E_{\mathrm{B},v',J+2}-E_{\mathrm{X},v,J+1})\right|. \quad (8)$$

This typically results in a value for Γ on the order of $0.16\,\mathrm{cm}^{-1}$, corresponding to a transform-limited pulse duration of about 200 ps in the time domain. The two transitions $|v,\ J\rangle \rightarrow |v',\ J+1\rangle$ and $|v+1,\ J\rangle \rightarrow |v'+1,\ J+1\rangle$ are not degenerate, primarily due to the anharmonicity of the vibrational potential. Note condition (8) is considerably more stringent than merely requiring the spectral component not to overlap with the nearest dipole-allowed rotational state, i.e. $\hbar\Gamma < |E_{\mathrm{X},\ v',\ J+1} - E_{\mathrm{X},\ v',\ J-1}|$. Adherence to (8) does not eliminate all undesired transitions, but empirically seems to keep the number small enough that most extraneous paths are removed by the selectivity of the S and P′ pulses.

In the most successful encoding scheme the S pulse contains 16 spectral components, roughly corresponding to the elements of the 4×4 matrix representing the two-qubit quantum gate. The spectral width of each component is chosen the same way as for the P pulse. In this scheme the selection of the next pair of vibrational levels is again unrestricted, although it may be helpful to choose them such that all four possible transitions from the first two vibrational levels have Franck–Condon factors of comparable magnitude. This is not strictly necessary, because the amplitude of each spectral component can be multiplied by a constant to compensate for the FC factor, although it does help to ensure that no single component is much stronger or weaker than the others. One might suspect that the S pulse should also include a phase correction to compensate for the free evolution the state has undergone since interaction with the P pulse, but this turns out to be unnecessary (see section 4.1). Finally, recall that the S pulse temporarily splits the rotational qubit into three separate states, which are later recombined by the P′ pulse (cf. figure 4(b)). The complex amplitudes chosen for the components that perform this splitting are such that the three levels can be recombined equally and in phase to produce the desired gate. This is illustrated in figure 5, which shows the rotational interferometer that will perform a unitary transformation on the rotational qubit specified by the matrix

$$\begin{pmatrix} A & B \\ C & D \end{pmatrix}.$$

Thus, the initial state $a_0|0\rangle_J + a_1|1\rangle_J$ goes to $(Ca_1+Da_0)|0\rangle_J+(Aa_1+Ba_0)|1\rangle_J$, given that the component of the S pulse connecting states $|J_0-1\rangle \rightarrow |J_0-2\rangle$ has relative amplitude (D–B), the one connecting $|J_0-1\rangle \rightarrow |J_0\rangle$ has amplitude B, and so forth. In addition, note that each rotational transition should be multiplied by a constant to compensate for the rotational matrix element of that transition. The four components of figure 5

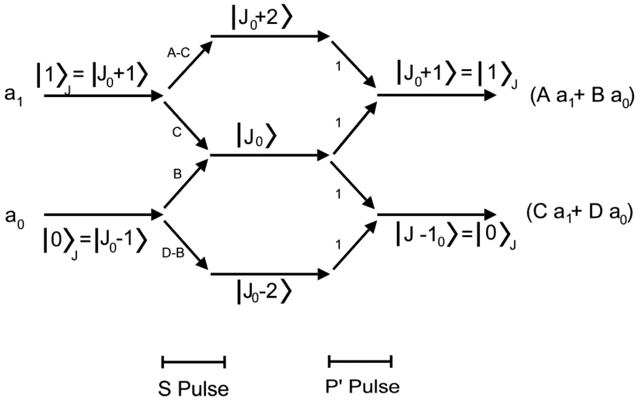

Figure 5. Encoding rotational state transformation.

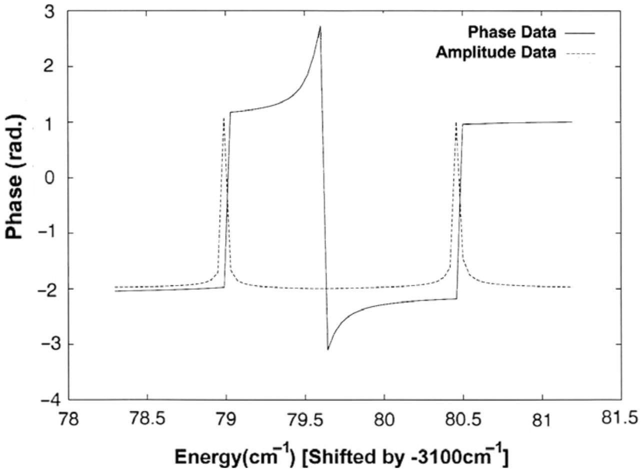

Figure 6. Simple anti-Stokes spectrum.

associated with the S pulse are all repeated four times, once for each possible vibrational transition. Each set of four is multiplied by a complex constant associated with the matrix element connecting the two states of the vibrational qubit.

The P′ pulse is the simplest of the three, consisting of eight spectral components with widths determined by the same criteria as for the P pulse. Apart from corrections for FC factors and rotational matrix elements, all components have equal amplitude. Corrections are made for FC factors and rotational matrix elements associated both with the transition induced by the P pulse, and the spontaneous emission events which produce the anti-Stokes signal. The pulse has only eight components because it does not perform any processing, so that transitions connecting the $|0\rangle_V$ with the $|1\rangle_V$ states of the vibrational qubit are unnecessary.

Readout is achieved by collecting the anti-Stokes radiation during a fixed time window, and computing its Fourier transform. It is important to ensure that the window begins only after the last pulse has finished interacting with the system, to avoid introducing errors in the phase data. The duration of data collection is typically ∼800 ps, corresponding to roughly 2^{19} grid points (where the time grid spacing is set by the duration of one half of an optical period). The time domain data are multiplied by a sinusoid at the transition frequency between the lowest states on the X and B electronic manifolds. This has the effect of shifting all the frequency components down by about $15\,000\,\mathrm{cm}^{-1}$, and greatly reduces the number of points required for an accurate transform. The final amplitudes of the qubits after the gate are read off by integrating the power spectrum over narrow intervals ($\sim 0.2\,\mathrm{cm}^{-1}$) around the expected transitions. The phases can be reliably determined from the argument of the complex frequency-domain data, the spectrum of which looks much as one would expect for a driven oscillator near resonance. An example of the amplitude and phase data for the rotational qubit is shown in figure 6. The state depicted has equal amplitude in both components and a relative phase of roughly zero. Hence it is approximately $|\psi\rangle \sim 2^{-1/2}(|0\rangle_J + |1\rangle_J)$.

Reading the phase data in the simulation corresponds to making a heterodyne measurement in the lab. Detection of the amplitude and phase of all peaks in the anti-Stokes spectrum gives a complete state tomography of the qubit density matrix. Thus, a single sequence of three pulses is sufficient to test the behaviour of the encoded gate for a given initial state. This fact is also useful when the goal is to implement a more complex quantum operation, consisting of the sequential application of multiple gates. In that case, the procedure is to apply one gate, record the resulting anti-Stokes spectrum, and then perform the following gate on a new thermal ensemble. The P-pulse of the second gate prepares an initial state in the new system exactly equal to the output state of the first gate. In order to properly interpret the anti-Stokes data, a calibration must be performed before every gate. This consists of a series of pulse sequences corresponding to $I_v \otimes I_J$ transformations on each of the four computational basis states. The calibration provides a reference with respect to which the phase of the AS radiation for the gate pulse sequence may be read.

4. Results and discussion

This section describes the main numerical results obtained with the TFRCARS simulation. Our primary focus has been to elucidate the experimental constraints on the optical fields required to generate, manipulate and detect the coherences used for encoding quantum information in this system. In subsection 4.1, we investigate the effect of uncertainties in the arrival times of the Raman pulses in the time domain, as well as in the time-gated detection scheme. Subsection 4.2 examines requirements on the frequency widths of each spectral component of a particular pulse, and hence on the resolution of the spatial light modulator used to generate the pulses. Finally, subsection 4.3 suggests how a multi-step quantum-processing task might be performed in the TFRCARS system, using the two-qubit Grover search algorithm as an illustration.

Much of the data in this section is displayed in terms of the fidelity of the observed quantum gate, plotted against the simulation variable of interest. For our purposes, fidelity is computed as the modulus of the inner product of the observed final state of the simulation with the output state expected from an ideal gate, *given a particular input state*. Symbolically,

$$F_{|\psi_i\rangle} = \frac{|\langle\varphi_{\text{exp}}|\psi_f\rangle|}{||\psi_f\rangle|^2}, \tag{9}$$

where $F_{|\psi_i\rangle}$ is the fidelity given input state $|\psi_i\rangle$, and $|\varphi_{\text{exp}}\rangle$ and $|\psi_f\rangle$ are the (properly normalized) expected output state vector, and the (un-normalized) observed output state.

A better description would minimize this product over all possible input states (see [28], p. 417). Unfortunately, performing the minimization over all inputs in two qubits would be numerically very time-consuming. Nonetheless, we expect that the present description should provide a reasonable qualitative picture. The best way to obtain the desired transformations is to eliminate or minimize the amplitudes of all extraneous paths through the state space. Empirically, the fidelities corresponding to the computational basis states alone should give a good idea as to whether this has been achieved.

4.1. *Requirements for pulse delays and time-gated detection*

Among the first questions one may consider using the TFRCARS simulation is that of the requirements on the precision in arrival times of the P, S, and P′ pulses necessary for implementing quantum operations with high fidelity. We found that, for pulses with sufficiently narrow spectral components (i.e. satisfying equation (8)), the observed anti-Stokes spectra are insensitive to changes in the time delays between the various pulses. Initially, this observation seems counterintuitive; in the usual picture of a two level quantum system, the relative phase between the states will oscillate in time if no interaction is imposed. In our perturbative formalism, however, it turns out that each pulse interaction effectively cancels the phase accrued during the free evolution period following the preceding pulse. As a simple demonstration, consider the case of two populated levels that undergo a free evolution starting at time $t=0$, and then interact with the applied field at t_1. Assume the pulse arriving at t_1 has two spectral components, designed to excite resonant transitions from initial states $|\phi_1\rangle$ and $|\phi_2\rangle$ to the final states $|\phi_1'\rangle$ and $|\phi_2'\rangle$ respectively. The frequency of level $|\phi_j\rangle$ is denoted ω_j. The final state $|\psi(t)\rangle$ is then given by

$$\begin{aligned}
|\psi(t)\rangle &= \int_0^t \mathrm{d}t_1\, \mathrm{e}^{-iH_{\text{free}}(t-t_1)/\hbar}\, \hat{\mu}\cdot(E_1(t_1)\,\mathrm{e}^{-i(\omega_1'-\omega_1)t_1} \\
&\quad + E_2(t_1)\,\mathrm{e}^{-i(\omega_2'-\omega_2)t_1} + \text{c.c.}) \\
&\quad \times \mathrm{e}^{-iH_{\text{free}}t_1/\hbar}(|\varphi_1\rangle + |\varphi_2\rangle) \\
&= \int_0^t \mathrm{d}t_1\, \mathrm{e}^{-iH_{\text{free}}(t-t_1)/\hbar}\, \hat{\mu}\cdot(E_1(t_1)\,\mathrm{e}^{-i(\omega_1'-\omega_1)t_1} \\
&\quad + E_2(t_1)\,\mathrm{e}^{-i(\omega_2'-\omega_2)t_1} + \text{c.c.}) \\
&\quad \times (\mathrm{e}^{-i\omega_1 t_1}|\varphi_1\rangle + \mathrm{e}^{-i\omega_2 t_1}|\varphi_2\rangle).
\end{aligned} \tag{10}$$

Roughly speaking, in the limit that the components at $(\omega_1'-\omega_1)$ and $(\omega_2'-\omega_2)$ are spectrally very narrow, the envelopes $E_j(t_1)$ may be represented as constants. The dipole operator acts on the state $|\phi_j\rangle$ to give $|\phi_j'\rangle$ only, again assuming the spectral width is narrow enough to give only one resonant transition. The remaining free evolution between t_1 and t (leftmost exponential under the integral sign above) can be replaced with $\exp(-i\omega_j(t-t_1))$ when acting on the state $|\phi_j'\rangle$, and the integration with respect to t_1 at long times $t \to \infty$ will eliminate the non-resonant cross-terms, so that the final result is

$$|\psi(t)\rangle = (\mu_1 \mathrm{e}^{-i\omega_1' t}|\varphi_1'\rangle + \mu_2 \mathrm{e}^{-i\omega_2' t}|\varphi_2'\rangle) + \text{c.c.}, \tag{11}$$

where the μ_j are scalar coefficients determined by evaluating the dipole operator for the relevant transitions. Thus, the duration of the free evolution between 0 and t_1 is irrelevant.

Note, however, that if the individual spectral components are modeled as Gaussian curves with standard deviations $\Gamma > (\omega_2 - \omega_1)$, then transitions $|\phi_1\rangle \to |\phi_2'\rangle$ and $|\phi_2\rangle \to |\phi_1'\rangle$ will also be excited. Then the analytical result of the integration is more complex to evaluate, but it is intuitively clear that integration of the Gaussian envelopes $E(t_j)$ will no longer eliminate the cross-terms, resulting in oscillations at $\pm(\omega_1 - \omega_2)$. Thus, the phase accumulation between pairs of states during free evolution is erased by the subsequent pulse, but only if the components of that pulse are sufficiently narrow.

Phase accumulation does occur after the third (i.e. P′) pulse of the sequence, since there is no succeeding interaction to undo it, and this has significant implications for reading out the result of a quantum operation in the TFRCARS system. As can be seen, for example, from equation (11), each final state of the computation oscillates in time, without further electromagnetic field interactions to cancel the phase accumulation. The contribution to the macroscopic polarization computed from any pair of these states (cf. equation (B.6)) will also be time dependent, and it is this that produces the observed optical field. In real experiments, phase data will most likely be measured with a time-gated detection scheme, as described in section 2.1. The phase-locked gate pulse must have a temporal length of several hundred picoseconds to resolve the spectral lines representing qubits from those of background transitions. As with the input pulses durations, this figure is equal to 2π divided by the frequency distance to the nearest undesired rotational transition, approximated in equation (8). The gate pulse used in the simulation is actually $\sim$790 ps, which is probably longer than necessary, but provides a convenient number of data points for numerical FFT calculation.

The procedure for quantum information processing in our TFRCARS simulations uses an initial calibration pulse sequence, corresponding to the ‘do-nothing’ $I_V \otimes I_J$ operation, to measure phase offsets caused by evolution of the coherence after the end of the P′ pulse. Such a calibration is only useful if the time window for data collection, determined by the gate pulse temporal width, is highly reproducible. One would expect the required precision to be something like the reciprocal of the largest energy difference in the problem, which is the level spacing of the vibrational qubit. Our numerical simulations included several tests to verify this.

Figure 7 shows a plot of fidelity versus the time-offset error in the delay of the data collection window for an $I_V \otimes H_J$ gate. The zero value on the horizontal axis corresponds to a window that follows the P′ pulse with exactly the same delay for both the calibration and the data run. (The actual value of the zero delay in this case is 715.2 ps, equal to four times the temporal width of the P′ pulse). Positive values on the horizontal axis indicate longer delays for the start of the data window than in the calibration. In all cases, the duration of the data collection is set to its default value of 790.0 ps. As expected, the plot shows oscillations with a period of $\sim$60 ps. This corresponds to the $\sim$1.1 cm^{-1} energy difference between levels of the rotational qubit, which is the largest in the output. In general, much faster oscillations should be visible, as the separation between vibrational levels is usually on the order of 100 cm^{-1}. However, for this gate and the initial states shown, the output state for the vibrational qubit is not a superposition, but always purely $|0\rangle_V$ or $|1\rangle_V$. Thus, only rotational beats are present. One may note that the fidelities for the $|v=0, J\rangle$ final states tend to diverge from those of the $|v=1, J\rangle$ states at large delays offsets. This is readily explained by the rotational–vibrational coupling in the molecular free Hamiltonian. Experimentally, gate delays on the order of hundreds of picoseconds may be controlled with femtosecond precision. Thus, it is expected that phase information can be read with great accuracy, even for output states that involve superpositions of the vibrational qubit.

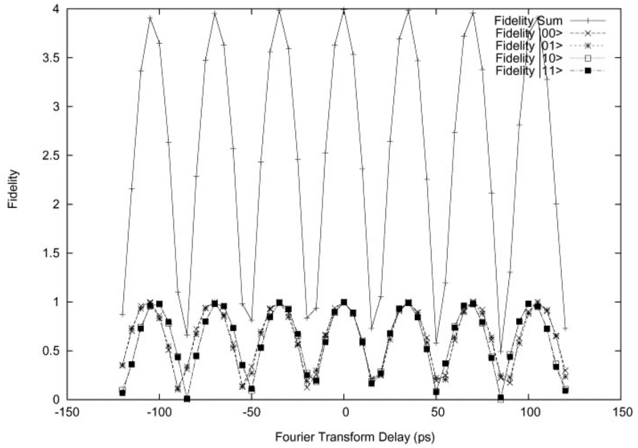

Figure 7. Fidelity vs. gate pulse delay error.

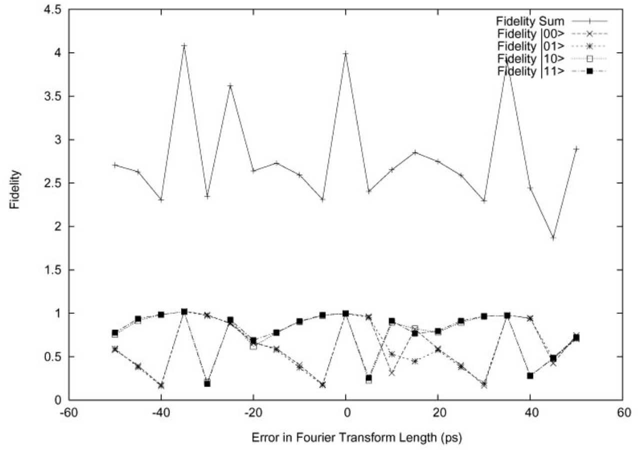

Figure 8. Fidelity vs. gate pulse duration error.

In addition to errors in the delay of the data collection window, one might also anticipate uncertainty in its duration. Figure 8 shows plots of gate fidelity, for the same $I_V \otimes H_J$ gate, against the error in the length of the gate pulse. Once again the error is applied only to the actual gate pulse sequences, not to the calibration. The start of the gate pulse is always 715.2 ps after the peak of the P′ pulse, and the error is added to the end of the window. In the previous case, the shape of the plot could be interpreted quite simply, since shifting the upper and lower bounds of the discrete Fourier integral together is just the same as pulling a complex phase factor out of each component. Here, one integration limit is varied while the other is held constant, and the resulting pattern is more complex. It seems to show some periodicity at about 35 ps, but the repetition on that timescale is obviously modulated. In any case, the thing to notice is that the region of high fidelity around zero delay is quite narrow, at less than 5 ps. Nonethless, the temporal width of the gate can be kept constant in experiments to within 10–100 fs for a given Kerr medium, which should be sufficient to avoid problems.

4.2. *Pulse spectral resolution and gate fidelities*

The spectral widths of the pulse components are a key consideration in obtaining the desired quantum gates. To the extent that spectral features are sufficiently narrow, only the necessary transitions are excited. No net phase evolution then occurs for the computational states between pulses, and the resulting transformation can be controlled exactly. If the widths become too large, however, extraneous paths begin to acquire significant amplitudes and can interfere with the result of the desired computation.

For this reason, a quantitative study of the influence of component widths on gate fidelity has been undertaken. The results presented here will concentrate on the representative examples of $H_V \otimes I_J$ gates, which display features characteristic of most data collected so far.

Figures 9(a)–(c) show plots of fidelity versus spectral width for $H_V \otimes I_J$. All four plots demonstrate fidelities fairly close to 1 for widths of up to about 1 cm^{-1}. This may be significant for practical implementations of the computing scheme, particularly in the case of the S pulse. The reason is that, according to [24], most pulse shaping experiments are limited to ratios of bandwidth/spectral feature size of a few hundred. Thus, resolutions of 1 cm^{-1} are probably attainable for the 331 cm^{-1} bandwidth S pulse, while the default value of ~0.2 cm^{-1} may not be. Limitations for the other pulses are less stringent.

The high-fidelity segment of figure 9(b) is shown on expanded axes in figure 10. For small linewidths, the calculated fidelities are consistently between 0.999 and 1.0. Because this behaviour persists to linewidths of almost zero, such data can be used to estimate an upper bound of about 0.001 on the numerical error in the computed fidelities. This error likely arises from integration on a finite time grid, as well as the early truncation of some numerical constants.

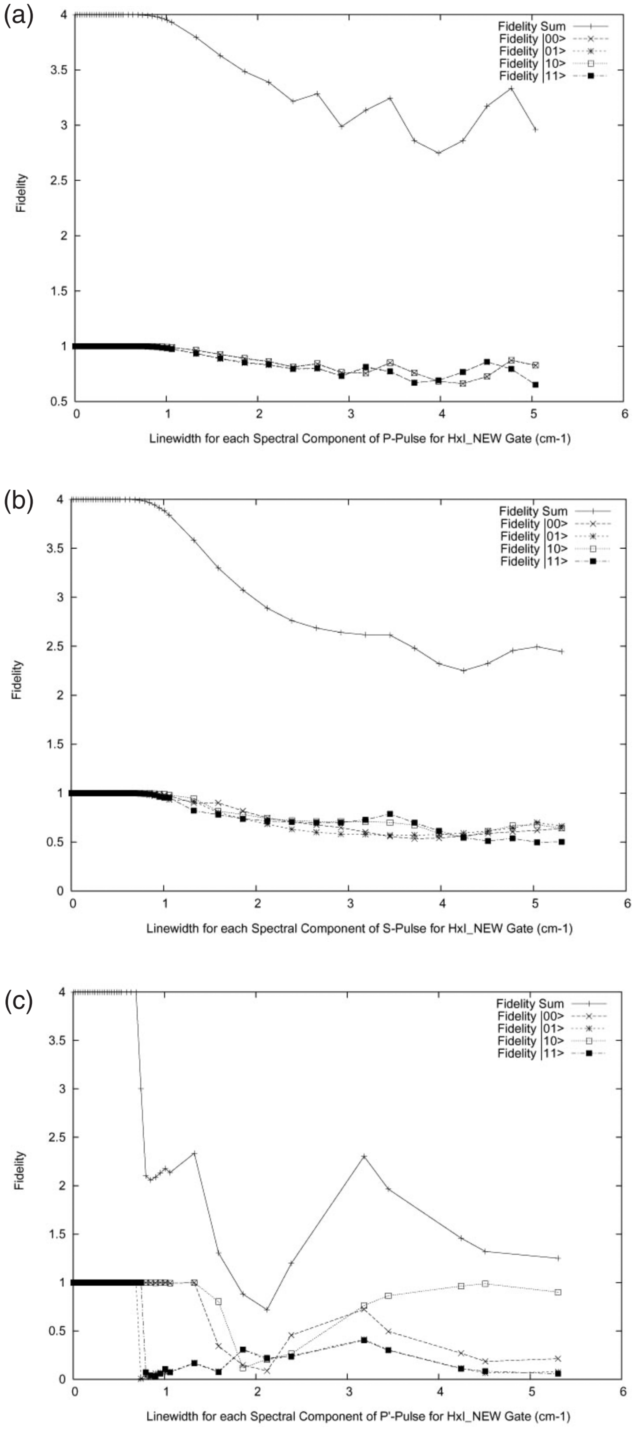

Figure 9. (a) Fidelity vs. spectral width of P pulse components of $H_V \otimes I_J$ gate. (b) Fidelity vs. spectral width of S pulse components of $H_V \otimes I_J$ gate. (c) Fidelity vs. spectral width of P′ pulse components of $H_V \otimes I_J$ gate.

Small inconsistencies in the bounds of integration for each peak in the anti-Stokes intensity spectrum may also contribute.

Note that the normalization of final states used to calculate fidelities in figures 9 and 10 is somewhat subtle, due to the fact that the operations performed on the qubits by the pulses in *perturbative* TFRCARS are not unitary. (This is, of course, a result of the fact that we are only considering the third-order coherence at the final step of the calculation; most of the amplitude associated with a given state before a perturbative pulse interaction remains in that state afterwards and does not contribute to the measured coherence. The total molecular wavefunction still evolves unitarily, as it must). When the frequency width of a particular pulse spectral component is sufficient to excite multiple resonant transitions from a given initial state, the amplitude of that state is not unitarily distributed between the final states. Paths leading out of and back into the space of qubits thus tend to cause the 'norm' of the computational wavefunction, experimentally observed as the intensity of particular lines in the anti-Stokes spectrum, to grow as component widths increase. Thus, in equation (9), the state vectors $|\psi_\mathrm{f}\rangle$ cannot be normalized independently, although the form of that expression still guarantees gate fidelities $F \leq 1$.

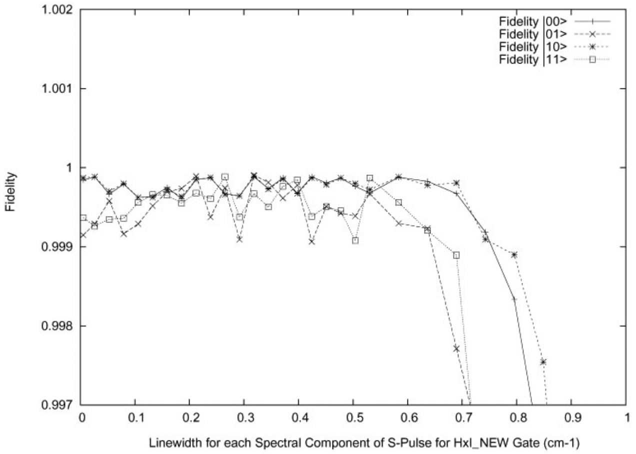

Figure 10. Fidelity vs. spectral width of S pulse components of $H_V \otimes I_J$ gate.

4.3. *Implementation of the Grover algorithm*

The execution of multi-gate quantum algorithms on the CARS system has been investigated in several simulations. Figure 11 shows the circuit diagram for the Grover search algorithm on two qubits. The Grover search problem concerns the identification of an element in a randomly ordered list. For example, imagine the problem of finding a single black ball in a box filled with $N-1$ white balls, subject to the constraint of not being allowed to look inside the box. You are allowed to take out one ball at a time. If a white ball is drawn it is tossed, and you continue until the black ball is found. Clearly, on average, the black ball is found after $N/2$ attempts. Grover [5] showed that a quantum computer can solve this task in $\sim N^{1/2}$ attempts. (For a rigorous description of how the algorithm works, see [5, 28]). The algorithm consists of the successive application of five quantum gates. Each gate is either a tensor product of single-qubit rotations or a controlled operation, and is implemented experimentally by a sequence of three pulses. Every gate is performed on a new thermal sample of iodine molecules. This is possible because the anti-Stokes radiation gives complete information about the qubit density matrix after the gate is applied. It can therefore, be recorded and used to design a P pulse that prepares an identical initial state for the next gate.

Figures 12–16 depict the pulse sequences for a two-qubit Grover algorithm as they might be observed in an experiment. For the sake of brevity, the calibration pulses for each gate have been omitted. The oracle for the computation has been designed to recognize the $|1_v\rangle \otimes |0\rangle_J$ state as a solution to the search problem. The first and second plots of each panel display the amplitudes of the three CARS input pulses, in the time and frequency domains, respectively. The amplitude of the S pulse is scaled by a factor of 10 for easier visibility. The S pulse is chosen to be weaker than the

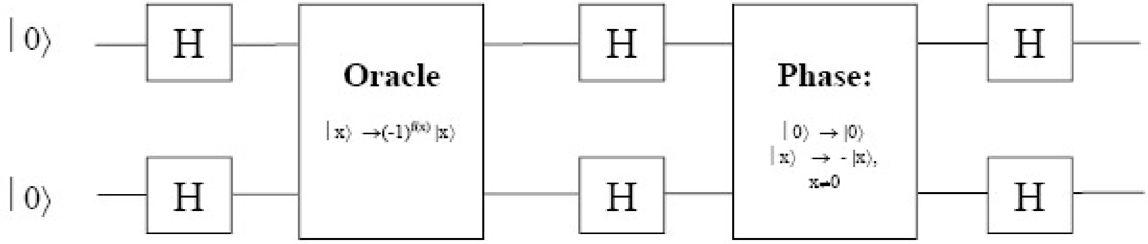

Figure 11. Circuit diagram for two-qubit Grover algorithm.

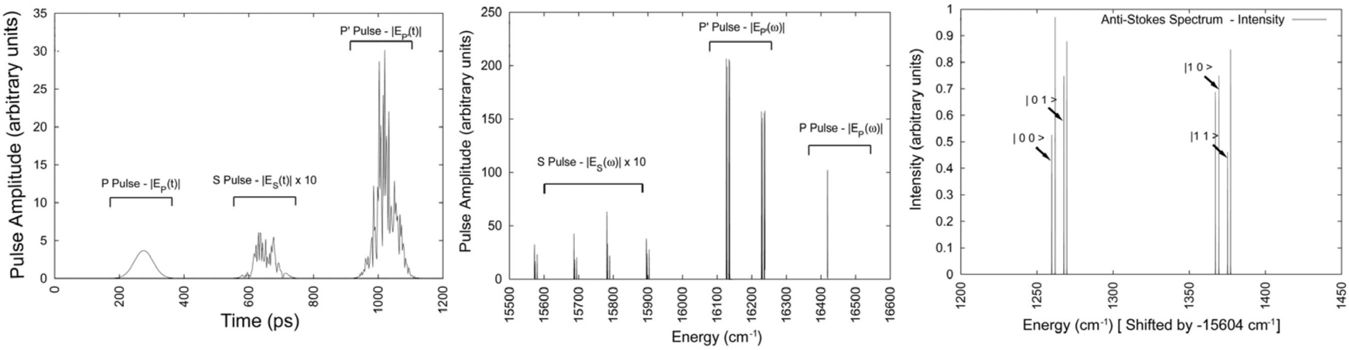

Figure 12. Data for first $H \otimes H$ pulse sequence.

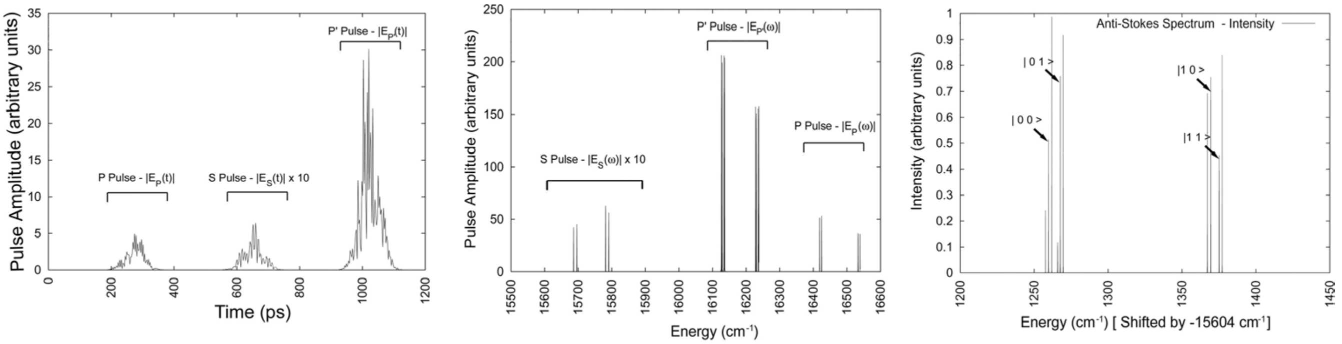

Figure 13. Data for oracle pulse sequence (selecting $|10\rangle$).

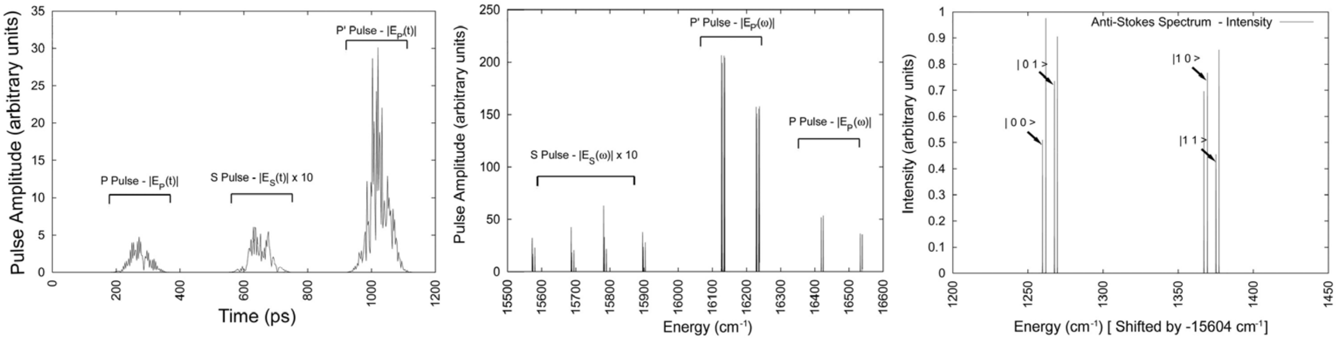

Figure 14. Data for second $H \otimes H$ pulse sequence.

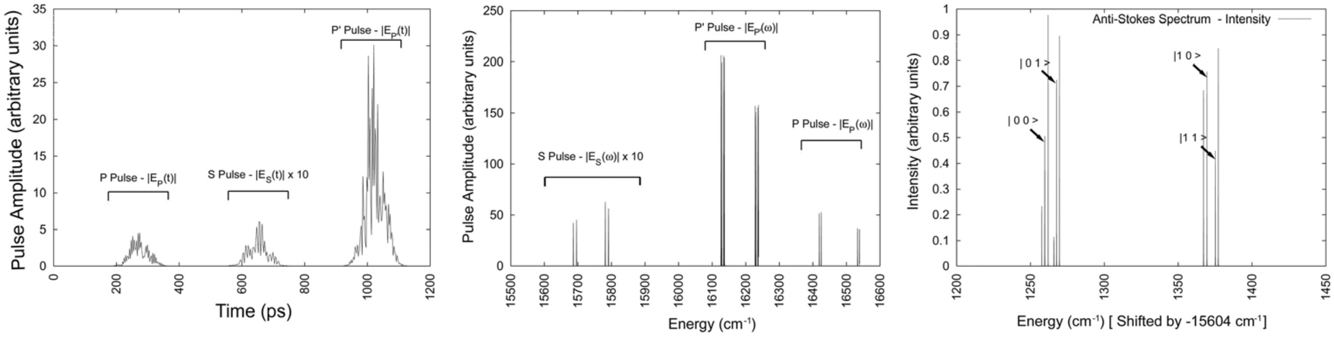

Figure 15. Data for selective phase gate pulse sequence.

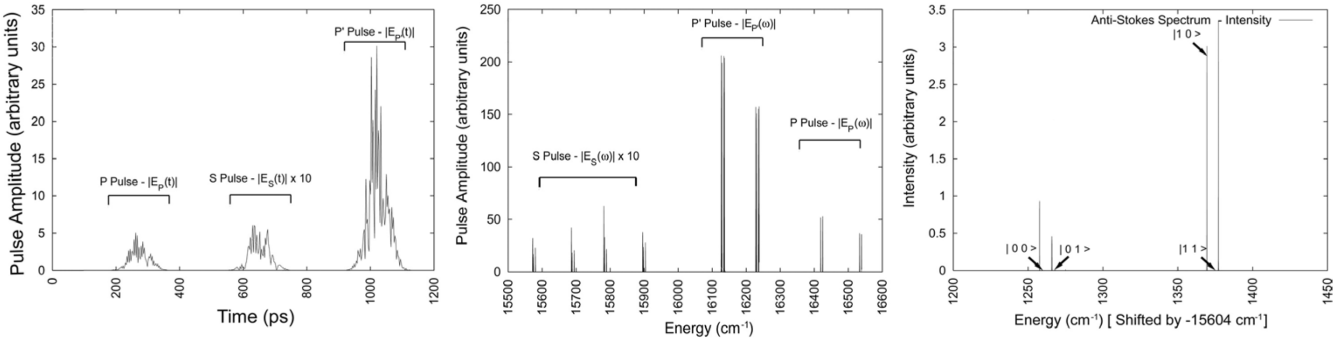

Figure 16. Data for final $H \otimes H$ pulse sequence.

others because it connects vibrational levels with relatively large FC factors in the present encoding. However, this is not fundamentally necessary.

The pulses are constructed using the method set out in section 3.1. Consider, for example, the pulse sequence shown in figure 13, representing the Grover oracle operation. The P-pulse, which is the first to arrive, consists of four spectral components, with component amplitudes selected to prepare the two-qubit state read off from the Anti-Stokes spectrum in figure 12. The component widths are sufficiently narrow that only the $|\mathrm{X}, v_0 = 0, J_0 = 52\rangle$ initial state undergoes excitation. The S-pulse, which arrives approximately 400 ps later, contains up to 16 spectral components, corresponding to the second set of diagonal arrows in the product of the two interferometers shown in figure 4. Amplitudes are selected to prepare the appropriate intermediate state for readout as illustrated in figure 5, as well as to compensate for differences in Franck–Condon factors and rotational matrix elements among the various paths through the state space. Note that many of the component amplitudes may turn out to be zero for a given gate; in this case the S-pulse has only six non-zero components. Finally, the P′-pulse arrives, after a delay of about 800 ps with respect to the P-pulse. It contains up to eight spectral components (although only four with non-zero amplitude in this case), which recombine the existing intermediate levels into the appropriate final state for the gate in the manner shown in figure 5. Again, each component is scaled appropriately to compensate for the relevant Franck–Condon factors and rotational matrix elements.

The third plot of each panel in figures 12–16 shows the intensity spectrum of the anti-Stokes radiation generated by the molecules. Lines in the spectrum corresponding to the qubits are located at 1261.7, 1267.4, 1369.2, and 1374.9 cm^{-1} for the states $|0\rangle_v \otimes |0\rangle_J$, $|0\rangle_v \otimes |1\rangle_J$, $|1\rangle_v \otimes |0\rangle_J$, and $|1\rangle_v \otimes |1\rangle_J$, respectively. These are read off at each step and used to generate the P pulse for the next gate. One could also show corresponding phase spectra for the anti-Stokes radiation; these too must be read to obtain a complete description of the qubits. The output spectrum at the end of the last step (third panel of figure 16) gives the final result of the computation. All peaks corresponding to qubits are suppressed, except the one at 1369.2 cm^{-1}. This is the correct solution to the search problem. Note that the doubling of the peak near 1370 cm^{-1} is quite deceptive, making it seem that the $|1\rangle_v \otimes |1\rangle_J$ state has finite amplitude. The pair has a splitting of roughly 7 cm^{-1}, and is therefore not indicative of the rotational qubit, which would be split by about 5 cm^{-1}. The higher-energy peak actually results from transitions between states outside the computational space. Careful inspection of the same region of the spectrum in figure 12 shows four peaks, two arising from $J \pm 1$ splitting of the $|1\rangle_v$ qubit, and two from transitions involving states outside the space.

The Grover calculation was also used to demonstrate the validity of describing the initial state of the system with a wave function, rather than a density matrix (c.f. section 2.2). Recall that this simplification was justified with the claim that, for a sufficiently selective P pulse, only one energy eigenstate in the thermal ensemble would contribute to the computation. The simulation was therefore performed repeatedly on initial states that had randomized phase relationships among their components in the energy representation. If the assertion that only one eigenstate participates is correct, then the simulation should give the same result independent of the relative phases. Figure 17 shows fidelities obtained for each computational basis state over ten repetitions of the Grover simulation. (Note that the actual algorithm always starts in the $|0\rangle_v \otimes |0\rangle_J$ state. Fidelities for other initial states are thus not generally of practical interest, outside of the present demonstration). Pulse component widths were set to the default 'safe' value of approximately 0.19 cm^{-1}. Amplitudes of components in the initial were Maxwell–Boltzmann distributed. From the calculated fidelities, as well as the

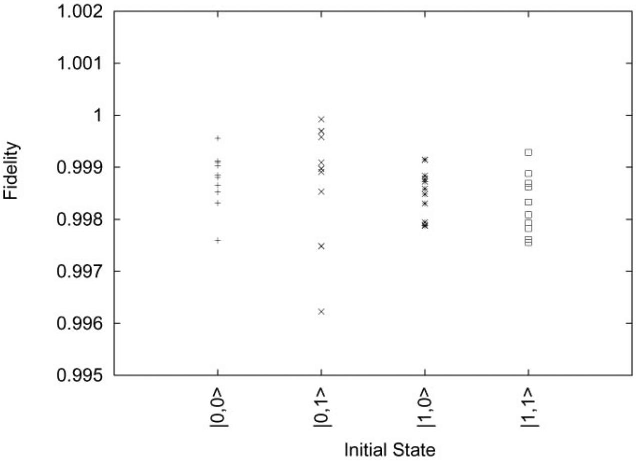

Figure 17. Grover fidelity scatter plot for random-phase initial states.

numerical elements of the matrix describing the complete Grover transformation, it seems that the randomization of initial state phases causes the output to fluctuate by less than about ~0.3%, which is comparable to the calculational uncertainties in fidelities estimated in the previous section. Thus, the use of wavefunctions to describe the state of the system is justifiable for realistic pulse widths.

5. Conclusions

TFRCARS in iodine vapour is a promising system for applications and for testing fundamental ideas in quantum information processing. This research has involved the development and simulation of a computation scheme that utilizes the Born–Oppenheimer separated tensor product space of the system. The encoding of qubits into molecular energy eigenstates, as well as the implementation of transformations by interaction with shaped pulses, can therefore be understood in terms of the standard circuit diagram representation for two-qubit quantum computation. A simple but important quantum algorithm, namely the Grover search algorithm, has been simulated.

Numerical investigations have yielded a number of potentially useful results. (i) It was found that for weak pulses with sufficiently narrow components, the phase evolution of computational states between pulses is effectively cancelled. This is surprising in itself, and can be used to compress the total time required for a computational step to the limits imposed by the effects of Doppler and collisional broadening on the anti-Stokes pulse. (ii) A study of the data readout procedure showed that precise timing of the Kerr-gate control pulse is critical to obtaining the desired transformations. (iii) It was confirmed that a key factor in determining the fidelity of the two-qubit gates is the spectral width of the components comprising each pulse. For the level encoding scheme tested, it was shown that gates have good fidelity for spectral widths of up to $\sim 1\,\mathrm{cm}^{-1}$. This is much larger than the lower limit set by the Doppler absorption width. It should be an achievable resolution, even if the maximum ratio of pulse bandwidth to component spectral width is limited by experimental considerations to a few hundred. (iv) The example of the two-qubit Grover search showed that the implementation of full quantum algorithms is possible. Cascading of gates is achieved by measuring the anti-Stokes pulse from one computational step and using it to prepare the pump pulse for the next step.

The present I_2 TFRCARS system is fundamentally limited to two qubits. It may be possible to extend this to three qubits, if the electronic state of the wavefunction can be harnessed in the strong field limit. Beyond this, the prospects for scaling up in the naïve way, by finding further Born–Oppenheimer separated degrees of freedom, are obviously limited. The system is therefore not of immediate interest as a cutting-edge quantum processor. Nonetheless, the relevant experimental technologies are already quite well developed, and the system has a number of favourable properties. This suggests that it might be useful in the short term for simple tasks in quantum information, possibly as an element in a quantum cryptography setup, or as a repeater or intermediate processing device in an optical quantum network. In the longer term, it may be feasible to increase the number of qubits in other ways. One idea involves changing from iodine vapour to a gaseous dimer consisting of many such symmetric tops, all weakly coupled via collective vibrations. A more promising proposal may be to imbed individual I_2 molecules in a solid argon matrix, allowing them to interact through phonons. Some experimental progress has already been made in this regard [16].

We conclude with a few suggestions for direct continuation of the present line of research. In preparation for experimental tests of the computation scheme, it would be useful to search for an optimal set of states for encoding the qubits. Such a set of states should have a large initial thermal population, small ratios of total pulse bandwidth to linewidths of individual spectral components, and approximately equal Franck–Condon factors for all transitions excited by a given pulse. Another future improvement is the analysis and reduction of sources of numerical error. This will be necessary to make very high-precision calculations of fidelities, which may be useful, for instance, in the context of fault-tolerance. Finally, it will be of interest to perform a completely new calculation, outside of the perturbative regime. Strong optical pulses will give rise to higher-order effects, which it may be possible to harness. In addition, they will allow for coherent superpositions of two or more electronic levels to be established. This may afford an additional qubit, in the electronic degree of freedom.

Appendix A: Pulse shaping

Precise control over pulse spectra is a key requirement in obtaining the transformations necessary for quantum computation. Experimentally, a spatial filtering apparatus is used to shape the pulses. The simplest case of such a filter consists of a pair of diffraction gratings and lenses, and a time-independent mask, as illustrated in figure A1. (The diagram, along with much of the discussion in this section, is condensed from Weiner's recent review paper [24]). The mask is located in the common inner focal plane of the two lenses, while the gratings are placed at the outer foci. The sequence of elements thus translates optical frequency → angle → position before filtering occurs, and then performs the reverse transformation afterwards.

The action of the mask can be understood in terms of the theory of linear filters. To the extent that the input femtosecond pulse is very short in time, the output field is simply described by the impulse response function of the filter. The electrical field immediately after the mask is a function of frequency, ω, and vertical position, x:

$$E_{\mathrm{m}}(x,\omega) \sim E_{\mathrm{in}}(\omega)\exp[-(x-\alpha\omega)^2/w_0^2]M(x), \qquad \text{(A1)}$$

$$\alpha = \frac{\lambda^2 f}{2\pi c d\cos(\theta_{\mathrm{d}})}, \qquad w_0 = \frac{\cos(\theta_{\mathrm{in}})}{\cos(\theta_{\mathrm{d}})}\left(\frac{f\lambda}{\pi w_{\mathrm{in}}}\right), \qquad \text{(A2)}$$

for α the spatial dispersion in units of length/angular frequency and w_0 the radius of the focussed beam impinging on the mask. The function $M(x)$ describes the ideal complex transmittance of the mask. The Gaussian factor arises from the diffraction-limited finite minimum spot size at the masking plane. In these equations, w_0 is the radius of the focussed beam at the masking plane, w_{in} is the beam radius before the first grating, c is the speed of light, d is the line spacing of the grating, λ is the optical wavelength, f is the focal length of the lenses, θ_{in} is the input angle at the first grating, and θ_{d} is the diffracted angle from that grating.

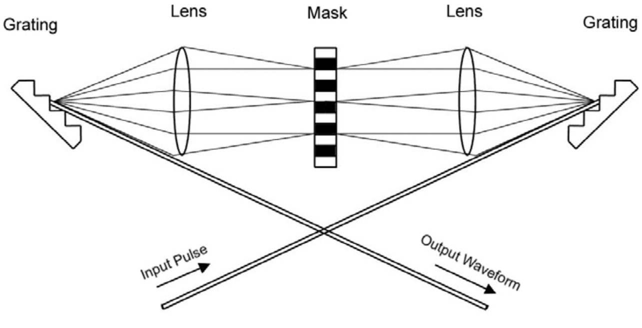

Figure A1. Basic pulse shaping apparatus (from [23]).

Spatial filtering must be performed in order to eliminate the position-frequency coupling in equation (A1) and obtain an output beam in a single Gaussian mode. This can be achieved by placing an iris after the final grating, effectively truncating the Hermite–Gauss expansion of $E_{\mathrm{m}}(x,\omega)$ at lowest order. The following filter function is thus obtained:

$$H(\omega) = \sqrt{\frac{2}{\pi w_0^2}}\int \mathrm{d}x\, M(x)\,\mathrm{e}^{-2(x-\alpha\omega)^2/w_0^2}. \qquad \text{(A3)}$$

Thus, the filter response is proportional to the ideal mask function, convolved with the intensity profile of the beam at the masking plane. For a filter consisting of narrow transmissive slits, $M(x)$ is a sum of δ-functions and $H(\omega)$ may be written as a sum of Gaussians with FWHM resolution $\delta\omega = (\ln 2)^{1/2} w_0/\alpha$.

One important figure of merit in optical pulse shaping experiments is the maximum number of distinct features that can be encoded into the available bandwidth, $\eta = B/\delta\omega$, where B is the bandwidth in units of angular frequency. Substituting (A2) into the expression for the feature size $\delta\omega$ and writing the bandwidth as $\Delta\lambda$ in units of wavelength gives

$$\eta = \frac{\Delta\lambda}{\lambda}\frac{\pi}{\sqrt{\ln 2}}\frac{w_{\mathrm{in}}}{d\cos(\theta_{\mathrm{in}})}. \qquad \text{(A4)}$$

Reasonable values for these parameters give η on the order of several hundred, which is close to the acceptable lower limit for producing the interferometers of figure 4 in iodine vapour. Increased complexities η could, in principle, be obtained by more elaborate schemes for dispersing the pulses.

Appendix B: Simulation details

The main issues in developing the numerical model of the TFRCARS system were: (i) the efficient storage of information describing the evolving quantum amplitudes of the iodine molecules in a large Hilbert space; (ii) the description of how the states evolve under the free molecular Hamiltonian; (iii) the procedure for computing the molecules' interactions with the electromagnetic field, as well as a proper description of the field itself; and (iv) the numerical evaluation of the triple-integral on an appropriate time grid, given that the duration of the simulation can be on the order of 10^6 optical periods. Complications such as multiple Liouville paths, permutation of overlapping pulses, and the need to allow for either absorption or stimulated emission at each interaction time, added to the overall complexity of the problem.

The code was written in C++, and most data structures were built from Standard Template Library (STL) objects. Extensive use was also made of the Matpack C++ numerics package, written by Berndt Gammel at Technischen Universität München [25]. Matpack code was used for the evaluation of Bessel functions and Clebsch–Gordan coefficients, for the computation of Fourier transforms, for finding the roots of complex polynomials, and for command-line parsing.

The perturbative calculation was performed strictly in the energy representation, using tabulated spectroscopic data. The main data structure used to describe the rovibronic wavefunction consisted of a list of integer triplets of the form $\{e, v, J\}$, each of which denoted a combination of eigenvalues corresponding to a tensor product of electronic, vibrational, and rotational energy eigenstates. A complex amplitude was associated with each triplet. The Hilbert space was limited to a slightly larger set of states than those likely to be reachable from the initial thermal ensemble: $e \in \{\mathrm{X}, \mathrm{B}\}$, $v \in \{0, 99\}$, $J \in \{0, 149\}$. To save on storage, the wavefunction was implemented as a list of only those basis states with non-zero amplitudes. The initial thermal state was truncated to include only states with normalized amplitudes greater than 0.01. This meant that the total number of states with non-zero amplitudes rarely exceeded $\sim 10^3$ out of the possible 3×10^4 in the space, unless the molecules were made to interact with very short (spectrally broad) optical pulses. Thus, the list implementation could be significantly more efficient than a simple three-dimensional array of quantum numbers.

In the energy representation, time evolution of the wavefunction was simply the traversal of the list of states and multiplication of each by $\exp(-\omega_{e,v,J}\Delta t)$. The spectrum, as well as Franck–Condon factors and rotational matrix elements used to calculate dipole matrix elements, were stored in external data files and loaded into memory at the start of the simulation.

In a preliminary calculation, Franck–Condon factors were determined by computing the overlap integrals of vibrational states in the position representation. The wavefunctions used for this purpose were eigenstates of four-parameter Morse potentials of the following form:

$$V(x) = D_\mathrm{e}(1 - \mathrm{e}^{-\beta(r-r_\mathrm{e})})^2 + V_0. \tag{B1}$$

The parameters $D_\mathrm{e}^\mathrm{X} = 12\,550\ \mathrm{cm}^{-1}$, $r_\mathrm{e}^\mathrm{X} = 2.666$ A, $\beta^\mathrm{X} = 1.858\ \mathrm{A}^{-1}$, $V_0^\mathrm{X} = 0$, and $D_\mathrm{e}^\mathrm{B} = 4500\ \mathrm{cm}^{-1}$, $r_\mathrm{e}^\mathrm{B} = 3.016$ A, $\beta^\mathrm{B}=1.850\ \mathrm{A}^{-1}$, $V_0^\mathrm{B} = 15\,647\ \mathrm{cm}^{-1}$ were used for the ground- and excited-state electronic potentials, respectively.

Hamiltonians corresponding to each potential were diagonalized in the position representation with the sinc-DVR method [26]. This amounts to using a global finite-difference approximation for the spatial second derivative, so that the kinetic energy matrix becomes

$$T_{i,i'} = \frac{\hbar^2(-1)^{i-i'}}{2m\Delta x^2} \times \begin{bmatrix} \pi^2/3, & i = i' \\ 2/(i-i')^2, & i \neq i' \end{bmatrix}. \tag{B2}$$

The potential energy is diagonal in the position representation, and the simple form of the Hamiltonian allows for easy diagonalization.

Energy levels were for the main TFRCARS calculation calculated from spectroscopic parameters tabulated in Herzberg [18], according to the parameterization for a non-rigid rotator:

$$\begin{aligned} E(e, v, J) = {} & \omega_\mathrm{e}(v + 1/2) - \omega_\mathrm{e}x_\mathrm{e}(v + 1/2)^2 + \omega_\mathrm{e}y_\mathrm{e}(v + 1/2)^3 \\ & + B_\mathrm{v}J(J + 1) + D_\mathrm{v}J^2(J + 1)^2 + E_0, \end{aligned} \tag{B3a}$$

with anharmonic vibration-dependent rotational constant

$$B_\mathrm{v} = B_\mathrm{e} - \alpha_\mathrm{e}(v + 1/2). \tag{B3b}$$

The values of the parameters were $E_0^\mathrm{X} = 0$, $\omega_\mathrm{e}^\mathrm{X} = 214.57\ \mathrm{cm}^{-1}$, $\omega_\mathrm{e}^\mathrm{X}x_\mathrm{e}^\mathrm{X} = 0.6127\ \mathrm{cm}^{-1}$, $\omega_\mathrm{e}^\mathrm{X}y_\mathrm{e}^\mathrm{X} = -0.000815\ \mathrm{cm}^{-1}$, $B_\mathrm{e}^\mathrm{X} = 0.03735\ \mathrm{cm}^{-1}$, $\alpha_\mathrm{e}^\mathrm{X} = 0.000117\ \mathrm{cm}^{-1}$, and $E_0^\mathrm{B} = 15\,641.6\ \mathrm{cm}^{-1}$, $\omega_\mathrm{e}^\mathrm{B} = 128.0\ \mathrm{cm}^{-1}$, $\omega_\mathrm{e}^\mathrm{B}x_\mathrm{e}^\mathrm{B} = 0.834\ \mathrm{cm}^{-1}$, $B_\mathrm{e}^\mathrm{B} = 0.0292\ \mathrm{cm}^{-1}$, $\alpha_\mathrm{e}^\mathrm{B} = 0.00017$. These parameters are consistent with the Morse parameters above to first order in $(v + 1/2)$, insofar as they satisfy the relation

$$\beta = \sqrt{\frac{2\pi^2 c\mu}{D_\mathrm{e}h}}\,\omega_\mathrm{e}, \tag{B4}$$

given the above values D_e of the dissociation constants (c.f. equation (B1)). Thus, the Franck–Condon factors calculated on Morse potentials in the first version of the simulation continued to be useful. Rotational matrix elements are simply sums of Clebsch–Gordan coefficients, which were determined with the aid of a Matpack library routine.

The optical pulses themselves were described as sums of Gaussians, to reflect the simplest possible phase mask, as outlined in the previous section. Each Gaussian was characterized by three parameters (complex amplitude, linewidth, and frequency-offset), and the pulse as a whole defined with respect to a fixed time origin. Evaluation in the time or frequency domain was performed by summation over the analytical expressions for each Gaussian. This can be slow for complicated pulses.

The triple integral that describes the contribution of a particular time circuit diagram to the macroscopic polarization was evaluated by decomposing the bra and ket into energy eigenstates, and integrating, starting with a particular eigenstate, over all the resonant paths through the Hilbert space. The results were then summed over the possible initial states, and the anti-Stokes dipole matrix elements evaluated. As an example, consider the time circuit diagram shown in figure B1. This diagram describes the case where the ket is acted upon with the P and P′ pulse-operators at t_1 and t_3, respectively, and the bra by the S′ pulse at t_2. Its contribution to the polarization may be written as

$$P_{\text{figure B1}}(t) = \int_{-\infty}^{t} \mathrm{d}t_3 \int_{-\infty}^{t_3} \mathrm{d}t_2 \int_{-\infty}^{t_2} \mathrm{d}t_1 \, \langle \psi_0 \Theta_{\mathrm{S}'}(t,t_2)|\mu|\Theta_{\mathrm{P,P}'} \times (t,t_3,t_1)\psi_0\rangle, \tag{B5}$$

where the operators Θ_j denote all electromagnetic field interactions and free propagations for the relevant intervals. Rewriting the initial state in terms of energy eigenstates $|\phi^{e,v,J}\rangle$, applying the Θ operators, and evaluating the integrals, one ends up with an expression which can be evaluated with tabulated dipole-matrix data:

$$P_{\text{figure 5}}(t) = \sum_{p,q} a_{pq}\langle\phi^{p}|\mu|\phi^{p}\rangle, \tag{B6}$$

where p and q are shorthand for an $\{e, v, J\}$ triplet. The first step in the evaluation of (B5) is to find the resonant paths through the Hilbert space for the bra and ket by evaluating the pulses in the frequency domain, and hence determining which basis states are included in the sums in (B6). For example, consider the simple case of the ket $|\psi_0\rangle = |\phi^{e=\mathrm{X},v=1,J=52}\rangle$, which will be denoted {X, 1, 52}. By doing a search through the spectral data for all dipole-allowed transitions, then comparing the energy differences to the evaluation of the P pulse in the frequency domain, it might be found that this state is resonantly connected to two others, say {B, 2, 51}, and {B, 2, 53}. The process is repeated for both of these states with the P′ pulse. The S pulse is not considered, because it acts on the bra in this diagram. Thus one arrives at one series of paths through the $\{e, v, J\}$ space for the ket, and another for the bra. The paths are grouped according to the states in which they terminate, and then the integrals are evaluated once for each path.

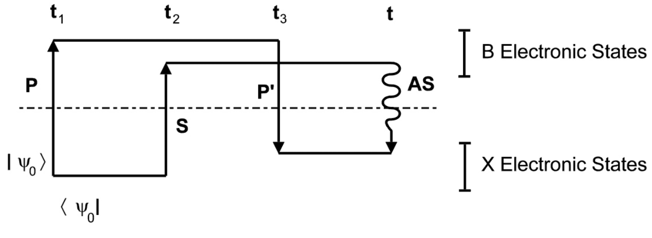

Figure B1. Sample time-circuit diagram.

Appendix C: Level encoding scheme

Unless stated otherwise, the following molecular eigenstates have been used to encode the qubits in our simulations:

$$\begin{aligned}
\text{Starting state: } & |\mathrm{X}, v=0, J=52\rangle \\
\text{After P pulse: } & |0,0\rangle \leftrightarrow |B, v=7, J=51\rangle \\
& |0,1\rangle \leftrightarrow |B, v=7, J=53\rangle \\
& |1,0\rangle \leftrightarrow |B, v=8, J=51\rangle \\
& |1,1\rangle \leftrightarrow |B, v=8, J=53\rangle \\
\text{After S pulse: } & |0,0\rangle \leftrightarrow |\mathrm{X}, v=3, J=52\rangle \text{ and} \\
& \quad |\mathrm{X}, v=3, J=54\rangle \\
& |0,1\rangle \leftrightarrow |\mathrm{X}, v=3, J=50\rangle \text{ and} \\
& \quad |\mathrm{X}, v=3, J=52\rangle \\
& |1,0\rangle \leftrightarrow |\mathrm{X}, v=4, J=52\rangle \text{ and} \\
& \quad |\mathrm{X}, v=4, J=54\rangle \\
& |1,1\rangle \leftrightarrow |\mathrm{X}, v=4, J=50\rangle \text{ and} \\
& \quad |X, v=4, J=52\rangle \\
\text{After P}' \text{ pulse: } & |0,0\rangle \leftrightarrow |B, v=11, J=51\rangle \\
& |0,1\rangle \leftrightarrow |B, v=11, J=53\rangle \\
& |1,0\rangle \leftrightarrow |B, v=12, J=51\rangle \\
& |1,1\rangle \leftrightarrow |B, v=12, J=53\rangle.
\end{aligned} \tag{C1}$$

These levels give maximum linewidths for all spectral components, when chosen to satisfy the criterion in equation (8), of around $0.19\,\mathrm{cm}^{-1}$. This substantially exceeds the Doppler absorption width of $\sim 0.013\,\mathrm{cm}^{-1}$

(FWHM, obtained using a Maxwell–Boltzmann distribution at $E_0 = 16\,000\,\mathrm{cm}^{-1}$, with $T = 323\,\mathrm{K}$ and $m_{\mathrm{I}_2} = 253.8$ amu). The Franck–Condon factors for all transitions excited by a particular pulse are of approximately equal magnitude, so that no spectral component is much stronger or weaker than the others. The mean transition frequencies are approximately $16\,477\,\mathrm{cm}^{-1}$ (606.9 nm), $15\,724\,\mathrm{cm}^{-1}$ (635.9 nm), and $16\,180\,\mathrm{cm}^{-1}$ (618.0 nm) for the P, S, and P′ pulses respectively, with total bandwidths of $120\,\mathrm{cm}^{-1}$ (4.4 nm), $331\,\mathrm{cm}^{-1}$ (13.4 nm), and $105\,\mathrm{cm}^{-1}$ (4.3 nm). While these properties are the most favourable of those observed with several trial level-encoding schemes, no rigorous search was performed to find a set of states that was in any sense optimal. If such a search were to be undertaken, useful criteria in selecting sets of states might include (i) large statistical amplitude of the starting state, (ii) small ratios of pulse bandwidth to the 'safe' spectral component width, (iii) equal widths for all spectral components within a given pulse, and (iv) equal (and large) Franck–Condon factors for all transitions excited by a pulse.

References

[1] R. P. Feynman, Int. J. Theor. Phys. **21,** 467 (1982).
[2] P. Benioff, Int. J. Theor. Phys. **21,** 177 (1982).
[3] D. Deutsch, Proc. R. Soc. London A **400,** 97 (1985).
[4] P. Shor, SIAM J. Comput. **26,** 1484 (1997).
[5] L. K. Grover, Phys. Rev. Lett. **79,** 325 (1997); Grover, Phys. Rev. Lett. **79,** 4709 (1997).
[6] D. G. Cory, *et al.*, Fortschr. Phys. **48,** 875 (2000).
[7] Q. A. Turchette, *et al.*, Phys. Rev. Lett. **75,** 4710 (1995).
[8] J. I. Cirac and P. Zoller, Phys. Rev. Lett. **74,** 4091 (1995).
[9] D. Vion *et al.*, Science **296,** 886 (2002); Yu *et al.*, Science **296,** 889 (2002).
[10] X. Li, *et al.*, Science **301,** 809 (2003).
[11] R. Zadoyan, *et al.*, Chem. Phys. **266,** 323 (2001).
[12] Z. Bihary, *et al.*, Chem. Phys. Lett. **360,** 459 (2002).
[13] J. Vala *et al.*, LANL, quant-ph/0107058 (2001); Amitay *et al.*, Chem. Phys. Lett. **359,** 8 (2002).
[14] V. V. Lozovoy and M. Dantus, Chem. Phys. Lett. **351,** 213 (2002).
[15] R. Zadoyan and V. A. Apkarian, Chem. Phys. Lett. **326,** 1 (2000).
[16] M. Karavitis, *et al.*, J. chem. Phys. **114,** 4131 (2001).
[17] S. Mukamel, *Principles of Nonlinear Optical Spectroscopy* (Oxford University Press, New York, 1999).
[18] G. Herzberg, *Molecular Spectra and Molecular Structure I* (Van Nostrand, Princeton, 1950).
[19] H. Haken and H. C. Wolf, *Molecular Physics and Elements of Quantum Chemistry* (Spinger, New York, 1995).
[20] R. N. Zare, *Angular Momentum* (Wiley, New York, 1987).
[21] G. Knopp, *et al.*, J. Raman Spectrosc. **31,** 51 (2000).
[22] S. Meyer and V. Engel, J. Raman. Spectrosc. **31,** 33 (2000).
[23] D. J. Tannor, *et al.*, J. Chem. Phys. **83,** 6158 (1985).
[24] A. M. Weiner, Rev. Scient. Instrum. **71,** 1929 (2000).
[25] http://www1.physik.tu-muenchen.de/~gammel/matpack/MATPACK.html.
[26] D. T. Colbert and W. H. Miller, J. Chem. Phys. **96,** 1982 (1992).
[27] C. Leforestier *et al.*, J. Comp. Phys. **94,** 59 (1991); R. Kosloff, A. Rev. Phys. Chem. **45,** 145 (1994); R. Kosloff, J. Phys. Chem. **92,** 2087 (1988).
[28] M. A. Nielsen and I. L. Chuang, *Quantum Computation and Quantum Information* (Cambridge University Press, Cambridge, 2000).